# A Short-Term Cloud Forecast Scheme Using Cross Correlations

THOMAS M. HAMILL AND THOMAS NEHRKORN

*Atmospheric and Environmental Research, Inc. Cambridge, Massachusetts*

(Manuscript received 1 February 1993, in final form 8 June 1993)

ABSTRACT

This paper describes a cloud forecast technique using lag cross correlations. Cloud motion vectors are retrieved at a subset of points through multiple applications of a cross-correlation analysis. An area in the first of two sequential frames of satellite data is correlated with surrounding areas in the second frame to find the one surrounding area best correlated. The location difference of the areas defines the displacement vector. An objective analysis is used to define displacements at every satellite pixel throughout the domain and smooth the local inconsistencies. Using these displacements, forecasts are then produced with a backward trajectory technique. This scheme was tested using two IR satellite images of the same scene a half-hour apart and found to generate realistic, high-quality forecast IR pixel images. Results demonstrate improvements over persistence and movable persistence for forecasts of a few hours' length. The technique is visually appealing, since forecasts are created in pixel images of the same form and resolution as the initializing satellite data, permitting animation. It is also computationally inexpensive.

## 1. Introduction

Cloud forecasting has been an active research area over the last decade, primarily because of the first-order influence of clouds on climate. Most of the operational weather forecast and climate models now include a diagnostic cloud forecast scheme. However, these schemes were tailored to produce realistic cloud amounts for forecasts on the order of days, not hours, and at resolutions on the order of 100 km. There are many users and potential users for shorter-range, high-resolution cloud forecasts. For example, military and civilian aviation need forecasts of obstructions to vision and information on weather affecting runway conditions. Television weathercasters may appreciate cloud forecasts that can be used to illustrate near-term changes to weather conditions. This article describes a cloud forecast scheme useful for such applications. Though originally developed for the U.S. Air Force Automated Weather Distribution System, a forecaster workstation, this forecast tool may be useful to a wider variety of users.

This short-range cloud forecast algorithm is based on the technique of lag cross correlations (Panofsky and Brier 1968). Using two sequential GOES IR images, cloud motion vectors (or "displacement vectors") are derived by correlating an area of the earlier image to surrounding areas in the later image. The area in the later image with the highest correlation is presumed to represent the displacement from the first image (Fig. 1). The technique has been used previously for satellite-derived winds (Merrill 1989), for cloud and rain forecasts (Bellon et al. 1992), and for radar-derived boundary-layer winds (Tuttle and Foote 1990). Using this basic building block of a cross-correlation analysis, an application of this technique to the production of IR cloud forecast images is described. Once the correlation analysis and subsequent objective analysis has defined a wind field, forecasts are made through a backward trajectory computation. The technique is suitable for short-range forecasts and can be run in a few minutes on current generation workstations. It is a mapping of a complex three-dimensional process to two dimensions, and as such, unduly simplifies the problem. As will be shown, it is at least a more appropriate simplification than other common computationally inexpensive alternatives.

This short-range forecast method is not compared against longer-range cloud forecast schemes here; it was specifically designed for nowcasting applications, (0–3 h), where advection is usually an appropriate first-order approximation. Beyond this length of time, development and dissipation generally become first-order effects. There are longer-range forecast schemes (e.g., Slingo 1987; Sundqvist et al. 1989; Mitchell and Hahn 1989) that implicitly account for this development and dissipation—schemes that typically require the execution of a dynamic forecast model. They have their own set of drawbacks, such as coarser spatial resolution, inaccuracy during the beginning forecast intervals due to model spinup, and dependence on relative humidity, which is notoriously difficult for numerical weather

*Corresponding author address:* Thomas Nehrkorn, Atmospheric and Environmental Research, Inc., 840 Memorial Drive, Cambridge, MA 02139.



© 1993 American Meteorological Society

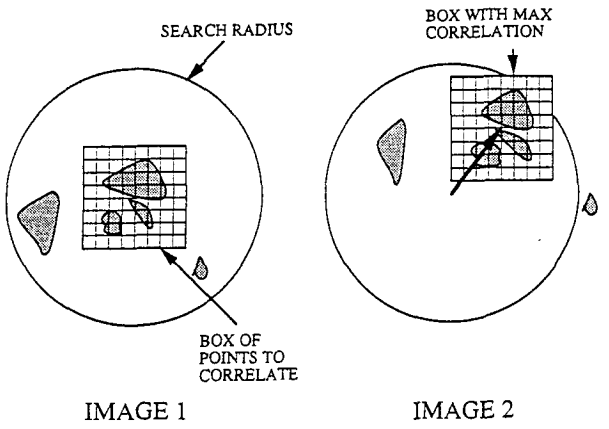


FIG. 1. Illustration of correlation analysis and derivation of the displacement vector. The displacement vector is directed from the center of the correlation box in image 1 to the center of the correlation box in image 2 most highly correlated with image 1.

prediction models to predict accurately. There is a crossover point between 3 and 18 h where these longer-range forecast schemes become more skillful than trajectory schemes. However, any crossover point for this scheme would be especially hard to determine since the output is a high-resolution pixel forecast, not a lower-resolution cloud amount forecast. Testing of the cross-correlations scheme was confined to a 0–2.5-h envelope; no comparisons are made with longer-range techniques.

Section 2 gives a detailed description of the forecast algorithm. Section 3 presents results from verification studies at both the large scale (central and eastern United States) and smaller scale (domains the size of states). Section 4 provides conclusions and recommendations for further enhancements.

## 2. Algorithm description

The cross-correlation technique has been applied to both large-scale forecast domains and smaller ones, with positive skill demonstrated for each. The algorithm for both is basically the same; the differences between large and small domain applications are the spacing between points selected for correlation analysis and the values of objective analysis parameters such as the influence radius. Specification of these parameters is delayed until the results section.

### *a. Retrieval and quality control of cross-correlations vectors*

At the heart of this prototype cloud forecast technique is the derivation of displacements vectors (i.e., "advective" velocities) through a cross-correlations analysis. The technique is as follows: a subset of pixels defining an area in the first image in a satellite loop is chosen. For the purpose of illustration in Fig. 1, this subset is 8 × 8; in our actual prototype scheme, the subset chosen is 15 × 15. Next, based on the maximum possible wind displacement in a half-hour, a search radius is defined and identically sized subsets of pixels from the second image with centers inside the search radius are correlated against the subset from the first image. If the scene has a single cloud layer, then the displacement vector for this layer will be defined by the vector from the center of the subset in image 1 to the center of the subset with the maximum correlation in image 2. This is illustrated in Fig. 1, and a sample plot of correlation coefficients and a derived displacement vector are shown in Fig. 2. This cross-correlations analysis is repeated at a regularly spaced subset of points throughout the domain, and displacement vectors for all points are then derived through an objective analysis.

As initially calculated, the correlations technique can derive vectors unsuitable for trajectory forecasts. There are three main problems requiring quality control (QC). 1) If small areas are used for the correlation analysis, the displacement vector may be inaccurate, reflecting a random high correlation and not a true advective wind velocity. 2) There may be multiple cloud layers, in which case a single displacement vector may not be applicable for that region (Leese and Novak 1971). 3) If the frame is clear, then the displacement vector will be null, even if strong winds are present through the clear scene. Use of the null wind in a trajectory forecast will prevent clouds from moving into the clear region.

The first problem, inaccurate vectors and resultant displacement field noisiness, can be corrected in many

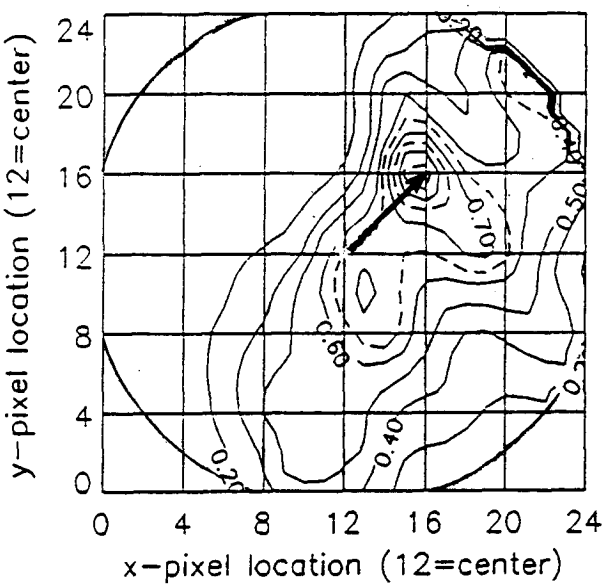


FIG. 2. Example of a correlation field used in the derivation of a displacement vector. The point (12, 12) is the center of the original correlation box. The displacement vector originates at this point and ends at the point with the highest correlation.

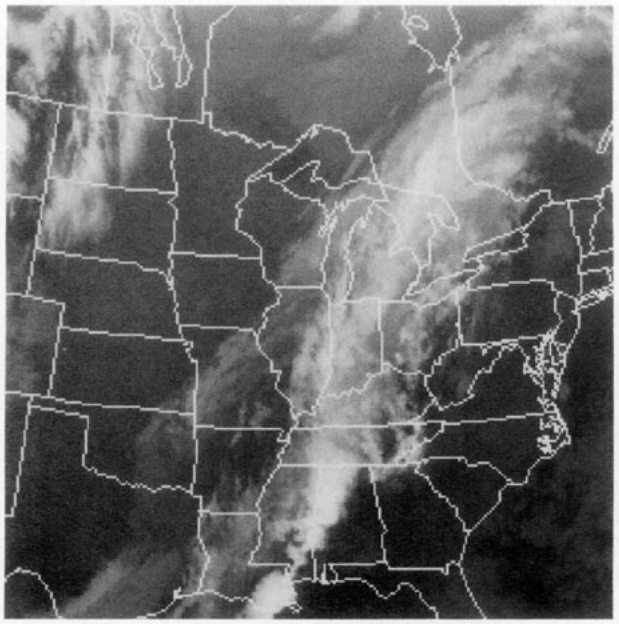

FIG. 3. A frame of the satellite imagery used in the demonstration correlation analysis. Data is over the central and eastern United States, valid at 1230 UTC 20 November 1991.

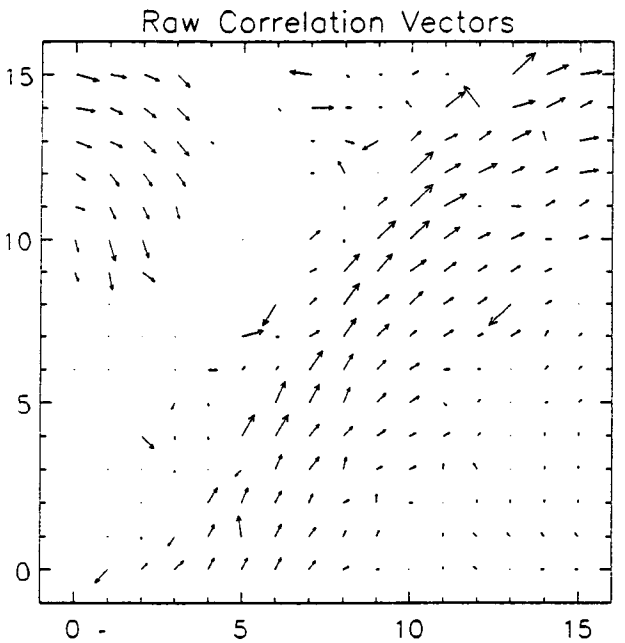


FIG. 4. A sample of the raw displacement vectors derived from two successive frames of GOES imagery, 1200 and 1230 UTC 20 November 1991.

ways. First, the size of area to correlate can be increased, decreasing the chance of a random maximum correlation. However, this increases computations. The choice of a 15 × 15 correlations area (here, with ~11-km pixel resolution) was a compromise between excessive CPU time and too many random vectors. Second, a local consistency check can be applied, comparing each derived vector against its neighbors. For this scheme, displacement vectors that deviate more than the width of four pixels from the local mean vector are replaced by the local mean. (Other deviations were tried, but four pixels gave the best result.) Figure 3 shows a frame of the remapped GOES IR satellite imagery used in the correlation (1230 UTC 20 November 1991). Figure 4 shows a field of correlation displacement vectors derived from data between 1200 and 1230 UTC 20 November 1991, illustrating typical noise. Figure 5 shows the same field of displacement vectors after application of the consistency check. This set of vectors is temporally consistent; for example, compare the results in Fig. 5 with those in Fig. 6, which shows the derived (and adjusted) vectors for the frames 0.5 h later, from 1230 and 1300 UTC imagery. A third possible correction for noisiness may be found through the use of a more sophisticated (and computationally intensive) cross-correlations algorithm. One such algorithm is the affine model (Fuh and Maragos 1991). This is a multidimensional minimization algorithm that not only finds the displacement with the highest correlation but also checks a range of image rotations and shape changes. This technique was not tried but may show promise in a few years with faster workstations.

Multiple cloud layers can seriously affect the accuracy of wind observations retrieved from satellite data (cloud-track winds). However, our focus is on pro-

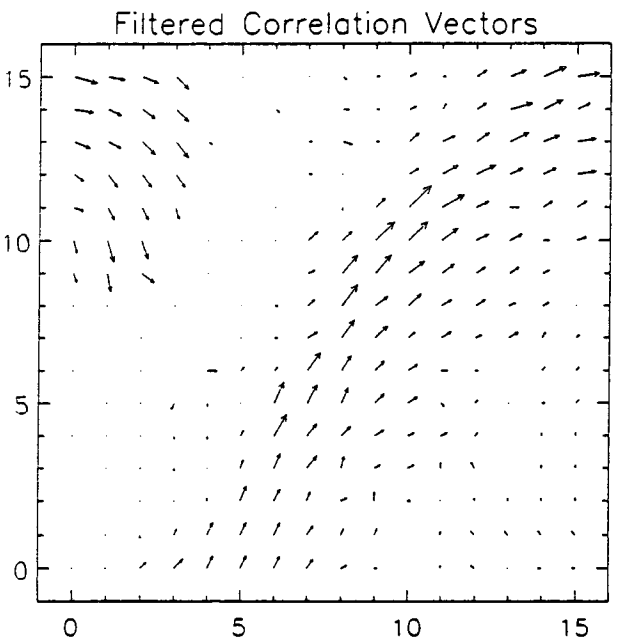


FIG. 5. Displacement vectors from Fig. 4 after quality control through a consistency check, examining and replacing wind vectors that deviate excessively from surrounding points.

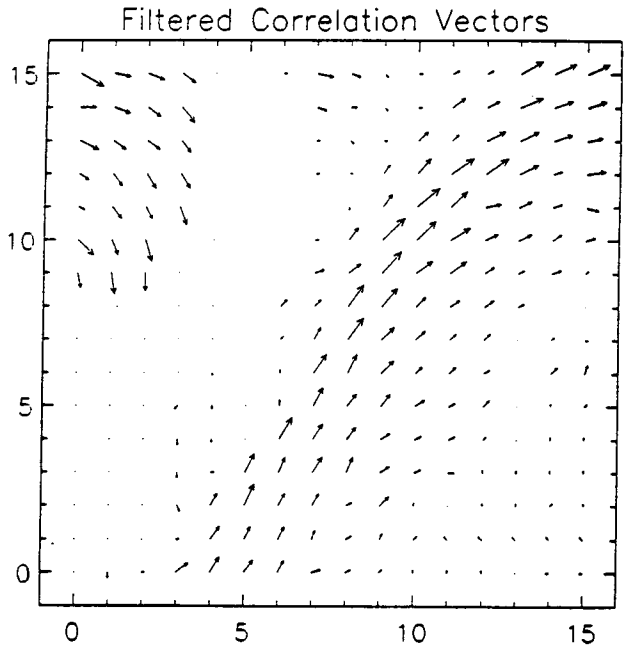


FIG. 6. Displacement vectors derived from images 0.5 h later (and processed through consistency check).

ducing a field of reasonable displacement vectors. A vector derived in a region with multiple cloud layers will usually be weighted to the cloud layer with the most contrast and will thus be most appropriate for forecasts of features discernible in the satellite imagery.

Null displacement vectors are derived when the analyzed subsets are cloud free. The movement of a cloud edge is often one of the most crucial features to forecast, and use of these null vectors in trajectory calculations will cause anomalous slowing of these features. Thus, a restriction is imposed during the objective analysis step, whereby null displacement vectors are removed from use as observations. As a result, advective velocities at cloud edges are not affected by null displacement vectors, and leading and trailing cloud edges are advected at more appropriate speeds. However, without correction, clear areas in front of the advancing clouds are also advected. This presents no problem when the clear-scene background is homogeneous, but prominent surface features such as lakes may appear to move. Though not attempted yet, this problem could be corrected through the identification of cloudy and clear pixels by a nephanalysis such as is done in Hamill et al. (1992). Cloudy pixels could then be explicitly forecast while clear pixels are persisted or replaced with a mask such as a colored background, as is often seen on commercial TV satellite loops.

Although there are drawbacks to defining advective velocities through a correlation analysis, there is one notable benefit. Assume there is only one cloud layer in a given area and advection (rather than development or dissipation) is dominant. If so, then a correlations-based scheme derives more reasonable displacement vectors than are achieved using an arbitrarily selected single-level wind such as a 500-mb wind field. Wind magnitudes generally increase with height, so by using the cross-correlations technique, areas of low cloud will have smaller magnitude displacement vectors than neighboring areas with high cloud. In essence, the trajectory wind field over the domain is appropriately warped to the local height of the clouds.

### b. *Objective analysis*

The next step after retrieval and consistency checking of displacement vectors is to produce gridded displacement vectors for every pixel in the domain. This is done by an objective analysis, chosen to smooth the vector field slightly and produce a continuous flow pattern. A multipass successive corrections scheme (Cressman 1959) is used. The first pass defines G1, the first guess at pixel $(i, j)$:

$$\mathrm{G1}(i,j) = \frac{\sum_{n=1}^{\mathrm{nobs}} [W^2 D(x_n, y_n)]}{\sum_{n=1}^{\mathrm{nobs}} (W)}. \quad (1)$$

Here, $W$ is the standard isotropic Cressman weighting function, dependent on the distance between the observation and the analysis point and a prespecified radius of influence (see section 3); $D$ is the displacement vector velocity for the observation at location $(x_n, y_n)$; and $U$ and $V$ components are analyzed separately in this process. The relation in (1) is used rather than the standard Cressman relation ($\Sigma (W*D)/\Sigma W$) to avoid discontinuities in data-sparse regions, as explained in Benjamin and Seaman (1985). The second pass corrects the first pass according to

$$\mathrm{G2}(i,j) = \mathrm{G1}(i,j) + \frac{\sum_{n=1}^{\mathrm{nobs}} \{W^2[D(x_n, y_n) - \mathrm{G1}(x_n, y_n)]\}}{\sum_{n=1}^{\mathrm{nobs}} (W)}, \quad (2)$$

where G2 represents the corrected analysis value. When a third pass is used, it is of the same form as the second pass, with G3 and G2 replacing G2 and G1, respectively.

The effect of eliminating null vectors from the objective analysis is illustrated in Figs. 7 and 8. Figure 7 shows an objective analysis of the data in Fig. 5 in which the null vectors are used. Figure 8 shows the implemented version in which the null vectors are deleted. As can be seen in the upper-left corner of the domain, the influence of the cloudy-area wind field is spread into the clear areas, resulting in stronger (more appropriate) magnitude winds along cloud edges. The

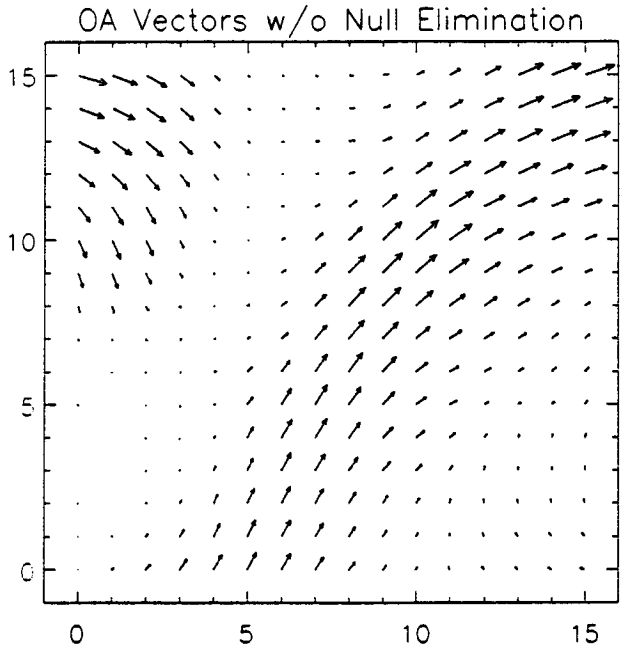


FIG. 7. Objective analysis of data from Fig. 5, without null displacement vectors eliminated.

scheme was tested out to 2.5 h; if the scheme is to be used for longer-range forecasts, the first-pass radius of influence should be increased to magnify the spreading effect.

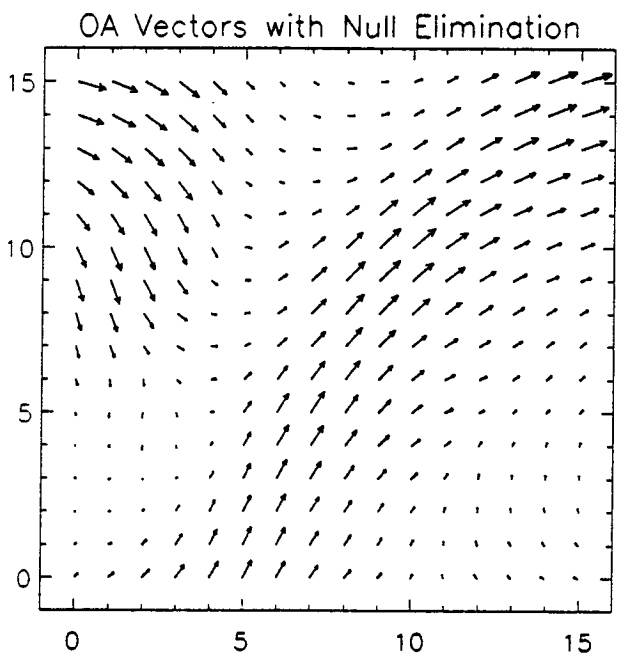


FIG. 8. Objective analysis of data from Fig. 5, with null displacement vectors eliminated.

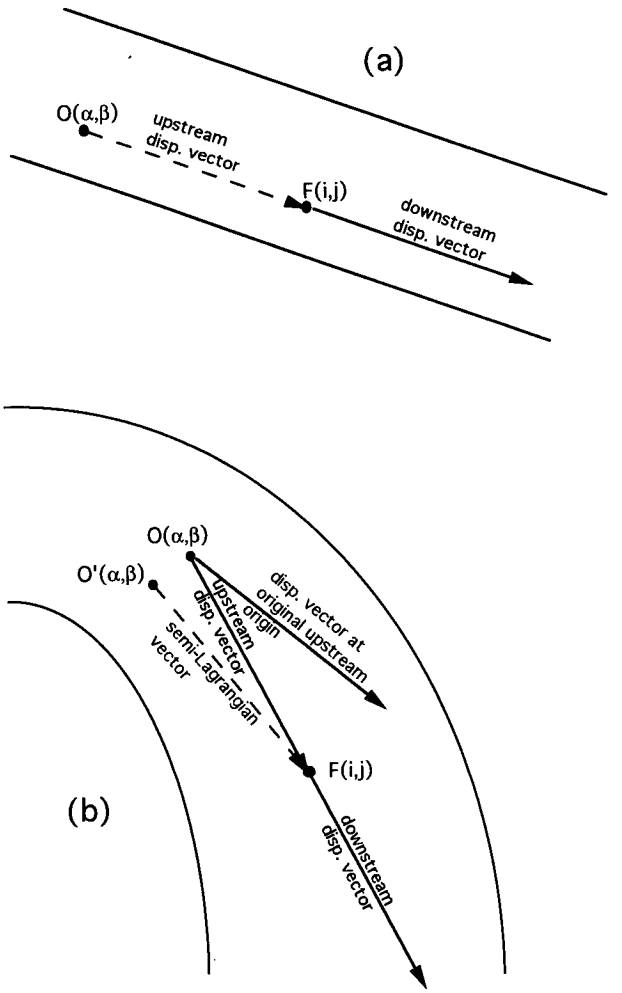


FIG. 9. Illustration of the inappropriateness of using cross-correlation displacement vector directly in curved flow. For straight, nondivergent flow (Fig. 9a), the displacement vector at $F(i, j)$ can be applied upstream to find the originating location of the trajectory $O(\alpha, \beta)$. However, in curved flow (Fig. 9b) the vector upstream is not identical, so a compromise vector $O'(\alpha, \beta)$ that does advect to $F(i, j)$ is determined through the semi-Lagrangian scheme.

### c. *Semi-Lagrangian trajectory forecast*

To produce forecast images, pixel intensities from the latest satellite image are advected using the analyzed displacement vectors. Before the trajectory technique is performed, however, the $U$- and $V$-component half-hour displacement vectors are modified slightly through a passive 2D semi-Lagrangian scheme (Staniforth and Cote 1991). The use of a semi-Lagrangian displacement vector rather than the original displacement vector itself markedly improves the trajectory forecasts in areas where the wind field at the trajectory end point differs significantly from the wind field at the trajectory origin, such as in curved flow. In essence, this scheme iterates to find the most representative half-hour trajectory. This is shown in Figs. 9a,b; in Fig. 9a, straight,

nondivergent flow allows the calculated downstream displacement vector at forecast location $F(i, j)$ to be applied upstream to find the originating pixel at $O(\alpha, \beta)$. However, as shown in Fig. 9b, in curved flow the displacement vector at the upstream location $O(\alpha, \beta)$ differs from the downstream displacement vector, so a compromise vector $O'(\alpha, \beta)$ that actually advects to forecast location $F(i, j)$ must be determined. The semi-Lagrangian technique iterates to determine this vector.

With corrected displacement vectors calculated, a simple backward-in-time trajectory is applied to the latest satellite data to make forecast images. For a backward scheme, the trajectory end points for time interval $t(i)$ are known; they are the regular set of grid points for the domain. Using the semi-Lagrangian vectors, the scheme finds the trajectory origin at time $t(i - 1/2$ h), and then a bilinear interpolation of the surrounding four pixel values is performed to determine the forecast pixel value. (Changes in brightness along the trajectory were tried as an additional predictor, but this did not improve the forecasts.) If the trajectory origin is outside the domain, the trajectory is assumed to originate at the nearest border point. The forecast scheme steps forward in half-hour intervals, with each successive forecast frame used in the initialization of the next step. The same velocity field and trajectory calculation is used for each forecast interval.

There are consequences from determining the forecast pixel value through bilinear interpolation. Though yielding a more accurate trajectory computation, its use results in a progressive smoothing of cloud features. The simplest alternative—rounding the trajectory calculation to the nearest pixel—would preserve sharpness of the original image but at the expense of a loss of accuracy. The use of bicubic splines rather than bilinear interpolation or the use of a noniterative trajectory technique may reduce or eliminate this problem, but these alternatives have not yet been tested.

Inaccuracies along the boundary are a natural consequence of a limited-area domain, and a daunting problem. The only proper solution is to widen the forecast domain and display only the model forecast for the inner, unaffected part. This would slightly increase the computational expense.

## 3. Results

Our prototype cloud forecast scheme has now been tested with satellite images over the central United States for each season. It shows skill over persistence for all time periods tested (0.5–2.5 h in half-hour increments). The scheme was also tested side by side with a similar advection scheme using the 500-mb winds, and comparison tests were made using a contour extrapolation method.

### *a. Comparison with persistence and 500-mb advection forecasts*

The domain used for the large-scale tests in this study is a Lambert conformal map projection covering the eastern two-thirds of the United States and southern Canada as in Fig. 3. Raw GOES IR imagery was remapped into a $256 \times 256$ set of pixels in this projection, with an approximate resolution of 11 km. Displacement vectors were calculated over a regular array of $16 \times 16$ points inside the satellite image, as illustrated in Fig. 4. A three-pass objective analysis was used, with the radius of influence set at 990, 660, and 440 km for the first, second, and third pass, respectively.

TABLE 1. Comparison of rms errors for 10-case ensembles of correlation, 500 mb, and persistence forecasts for each of the four seasons, and for each forecast interval. Units are gray-shade values, which range from 0 to 256 in the original imagery

| Forecast hour | Season | Correlation rms | 500-mb rms | Persistence rms |
|---|---|---|---|---|
| 1/2 | Fall | 9.13 | — | 12.32 |
| | Winter | 8.57 | 9.36 | 11.30 |
| | Spring | 8.98 | — | 11.95 |
| | Summer | 11.28 | 11.63 | 13.96 |
| 1 | Fall | 12.87 | — | 16.21 |
| | Winter | 11.67 | 12.82 | 14.98 |
| | Spring | 12.55 | — | 16.04 |
| | Summer | 16.32 | 16.99 | 19.77 |
| 1 1/2 | Fall | 15.35 | — | 18.59 |
| | Winter | 14.19 | 15.22 | 17.38 |
| | Spring | 14.99 | — | 18.55 |
| | Summer | 19.94 | 20.61 | 23.46 |
| 2 | Fall | 17.27 | — | 20.48 |
| | Winter | 16.12 | 17.09 | 19.23 |
| | Spring | 17.02 | — | 20.51 |
| | Summer | 22.77 | 23.44 | 26.36 |
| 2 1/2 | Fall | 18.95 | — | 22.16 |
| | Winter | 17.79 | 18.64 | 20.83 |
| | Spring | 18.64 | — | 22.19 |
| | Summer | 25.25 | 25.82 | 28.78 |

The pixel forecasts were then compared against the verification images over the full domain, including areas contaminated by boundary condition errors. An ensemble of 40 forecasts, 10 for each season were made, and rms errors (in pixel gray-shade values) were calculated using the observed satellite imagery for verification. Summed over all four seasons, there was an even split between daytime and nighttime forecasts. Verification in pixel gray-shade values is convenient for calculation, but because of the change in sensitivity in GOES IR count at $-22$°C (i.e., change in brightness temperature per gray shade), by using this there is a bias of the rms errors toward performance of the higher clouds, in terms of coverage. With this in mind, rms errors of the correlations forecasts and of persistence were compared. For all tests and all times, the correlations-based advection scheme showed less rms error than persistence (Table 1). As shown, both persistence and the correlation method exhibit higher errors in summer than in winter. From visual inspection of the cloud forecasts, this was clearly due to the dominance of convective development and dissipation over advection during the summer months. Conversely, during

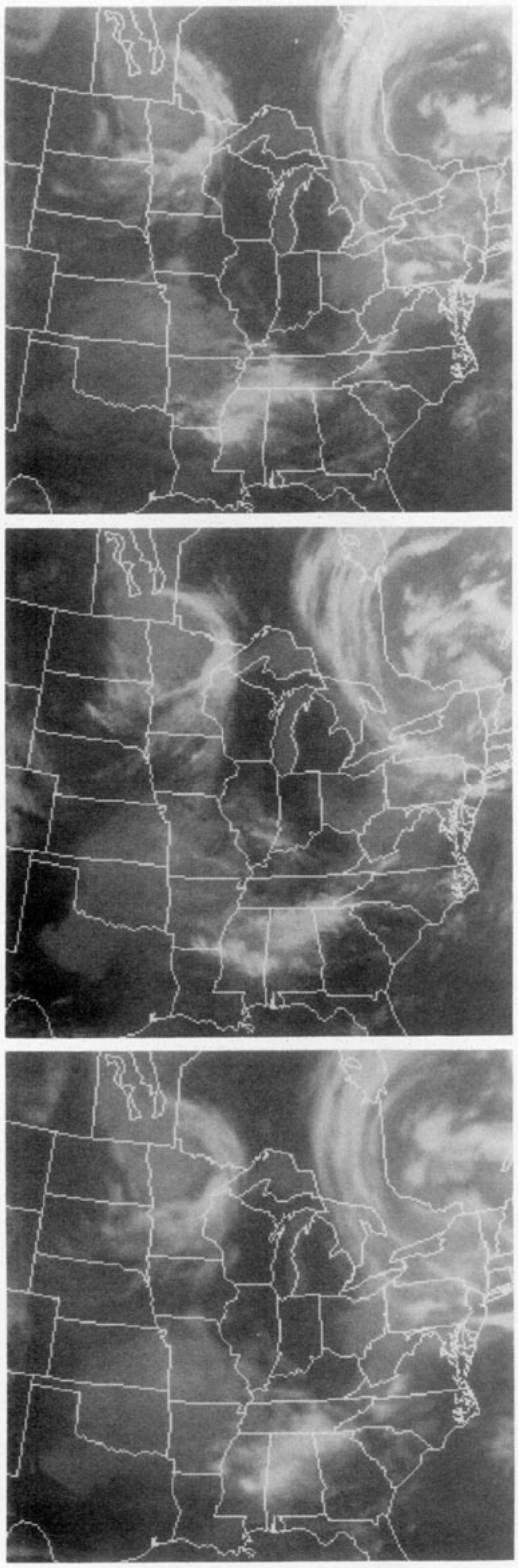

FIG. 10. Satellite analysis (top), verification (middle), and 2.5-h correlation forecast (bottom) started from data at 1430 UTC 20 April 1991.

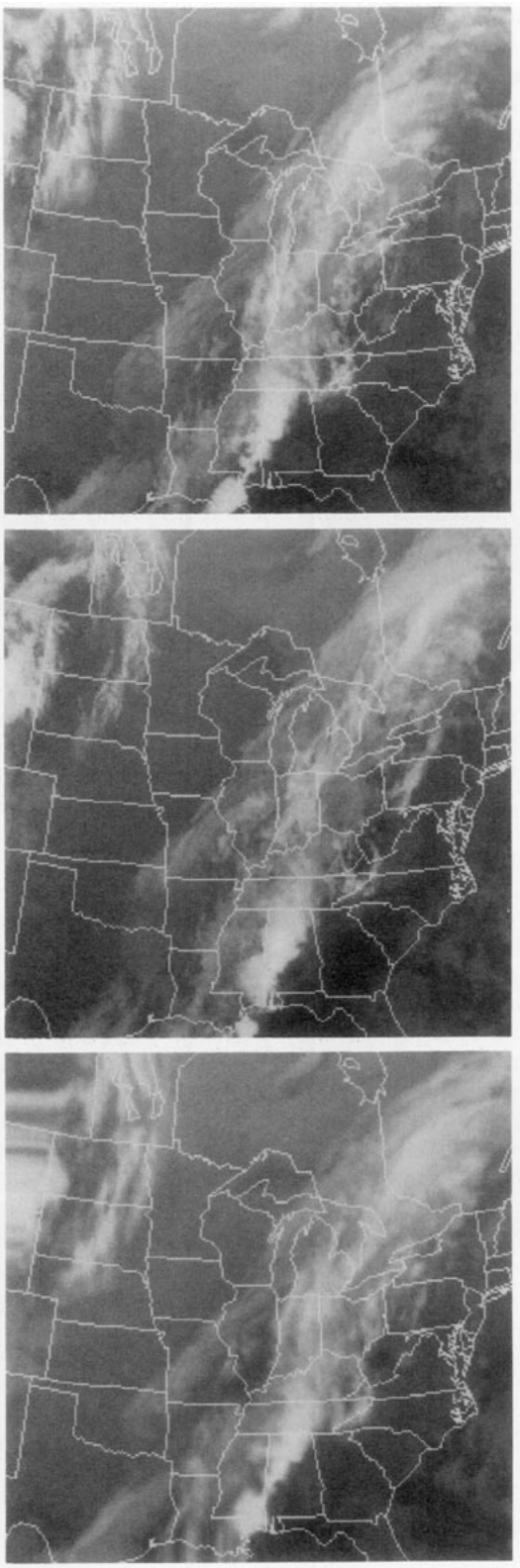

FIG. 11. Satellite analysis (top), verification (middle), and 2.5-h correlation forecast (bottom) started from data at 1430 UTC 1200 UTC 20 November 1991.

the winter, advective processes seemed to dominate, and both persistence and the correlations technique show smaller errors, and the *percentage* improvement of correlations-based forecasts over persistence is greater in winter than in summer.

Figures 10 and 11 show examples of two forecasts, along with the initial conditions and verification data. Close examination shows that there are noticeable differences between the forecast and verification satellite data, though the basic propagation of features is handled well. The terrain advection problem can be seen in Fig. 10 bottom, where Lake Michigan appears to move. Figure 11 bottom illustrates the problem of boundary conditions; the northwest corner is improperly forecast due to strong cross-boundary flow into the domain.

A reasonable alternative candidate to a correlations-based forecast scheme is one using 500-mb winds for displacement vectors (Nagle 1992). This option was tested for the winter and summer cases (Table 1). The correlations forecasts are clearly superior in the winter but much closer to the rms of the 500-mb forecasts in the summer. The generally higher rms in the summer and the smaller rms difference between correlations and 500-mb forecasts for summer cases is most likely due to the dominance of convective development and dissipation. During the summer, use of the 500-mb wind field as a steering current for thunderstorms generally makes as much sense as correlations-derived winds, which cannot be expected to produce reliable wind vectors in regions of development and dissipation. Conversely, during the winter months, the correlation scheme's ability to determine an accurate advecting velocity regardless of the height of the cloud is likely responsible for its higher skill.

Since synopticians may often use a fraction of the 500-mb wind velocity for the phase speed, it seemed appropriate to determine if lower-elevation winds might yield more accurate forecasts. A few forecasts were made using 700-mb winds instead of 500 mb; the verification scores for this small sample were generally worse. Forecasts with smoothed 500-mb fields were not tried nor were combinations of 500-mb wind analyses and correlation analyses nor the use of upper-air analyses for a first guess in the objective analysis. Though intuitively many of these ideas are defensible, this research was originally designed to meet U.S. Air Force needs for a forecast system that can be run at locations where only satellite data is available. Applications for data-rich environs may profit from the judicious inclusion of upper-air winds.

### b. *Contour extrapolation scheme comparison*

Other techniques exist for determining the evolution of prominent cloud features, such as contour extrapolation methods (Heideman et al. 1990). If a forecast subdomain is dominated by one cloud feature, then the short-term movement can be forecast by bounding the feature with a contour at a given pixel brightness, contouring the feature, and linearly extrapolating the feature using the change in centroid position. Figure 12 illustrates a sample case, showing the contours overlaid on satellite imagery. Movement in successive forecast frames is defined from the change in centroid

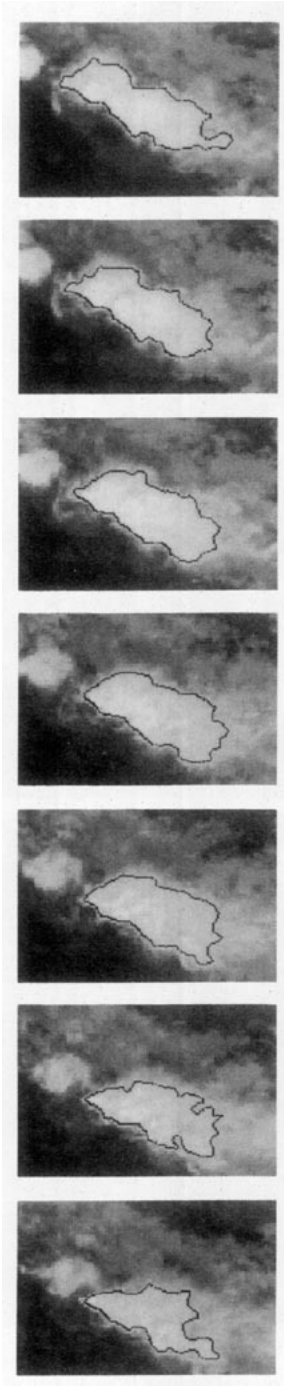

FIG. 12. The 0.5-h satellite data starting at 1500 UTC 20 November 1991, over Alabama–Mississippi, illustrating the bounding of a region of significant weather with contours. Contours correspond to brightness temperature 237.5 K.

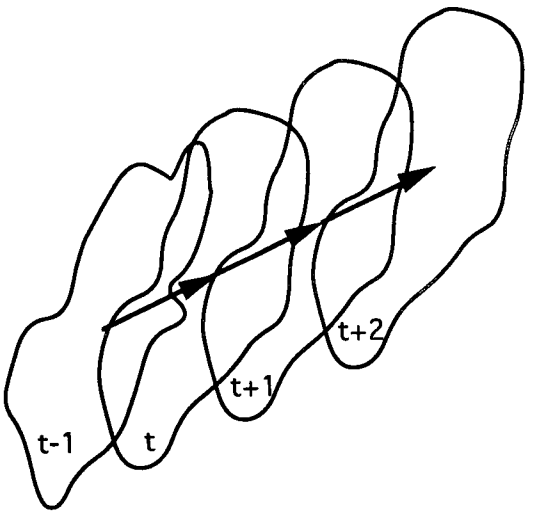


FIG. 13. Illustration of movable persistence contour forecast. The change of center of mass from time $(t-1)$ to $(t)$ is used to define a motion vector, and the shape at time $(t)$ is used as the shape for successive forecast frames at times $(t+1)$, $(t+2)$, etc.

position between frame 1 and frame 2, and the shape and size from frame 2 is preserved in successive forecast frames. This is illustrated in Fig. 13. More details on this "movable persistence" scheme and comparisons with other contour forecasting schemes are discussed in Nehrkorn et al. (1993). One of the conclusions of that report was the superiority of simple movable persistence over more elaborate contour-based schemes, which attempted to forecast shape and size changes as well. Thus, the accuracy for correlations forecasts was compared against the best alternative, simple movable persistence.

For this comparison, a four-season database of 39 significant weather features was chosen, approximately 10 from each season, again, roughly split between half-day (1200–0000 UTC start time) and half-night (0000–1200 UTC). For each case, the satellite loop was examined for an interesting feature. A subdomain around the feature and a contour level bounding the feature were defined, and then results of the contour analysis were stored for initialization and verification. The satellite loop examined for case selection used the same domain as the previously mentioned large-scale forecasts, though the domain resolution was doubled to approximately 5.5 km and the size doubled, to 512 $\times$ 512, for easier visualization. If there were extraneous, smaller contours besides the main feature of interest, they were disregarded in calculating centroids and defining the displacement vector. Movable persistence forecasts for the satellite image were then derived by extrapolating the movement of the whole image with the displacement vector calculated from the change of the centroid position.

The correlations forecast scheme was modified to work over the smaller domain and produce a displacement wind analysis with somewhat finer-scale structure than the coarse analysis from the synoptic-scale tests. This was done in two ways: first, the spacing between points for calculation of displacement vectors was reduced; actual spacing varied with the size of the subdomain. Next, the objective analysis was tuned to yield more detail. A three-pass objective analysis was used with influence radius that varied with domain size; the first pass was 15 times the spacing between correlation analysis vectors, the second pass 10 times the spacing, and the third pass 6 times.

Movable persistence forecasts were then compared against the cross-correlation forecasts. For comparison of forecast accuracy, contingency-table-based skill scores were used (Stanski et al. 1989) rather than pixel rms. Our measurement criteria were the critical success index (CSI), probability of detection (POD), and false alarm ratio (FAR). Using the breakdown of areas shown in Fig. 14, the scores can be defined as follows:

$$\mathrm{CSI} = A/(A+B+C) \tag{3}$$

$$\mathrm{FAR} = C/(C+A) \tag{4}$$

$$\mathrm{POD} = A/(B+A), \tag{5}$$

where $A$ represents the cloud pixels correctly forecast, $C$ represents false alarms (forecast, no verification), and $B$ represents the misses (verification, no forecast). Scores for CSI, FAR, and POD range from 0.0 to 1.0; high CSI and POD are desirable, as is a low FAR.

Graphs of mean CSI, FAR, POD as functions of forecast time are shown in Figs. 15–17 with 5% confidence intervals. As shown in Fig. 15, the CSI scores for correlation forecasts are significantly better on average than movable persistence scores for 0.5- and 1-h forecasts, and they continue to exceed the skill of

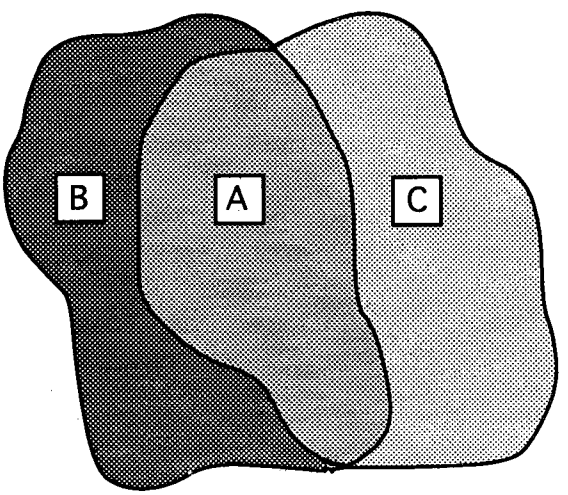


FIG. 14. Illustration of two contours bounding a forecast area $(C+A)$ and a verification area $(B+A)$, and the breakdown into regions of hits (area $A$), false alarms (area $C$), and misses (area $B$).

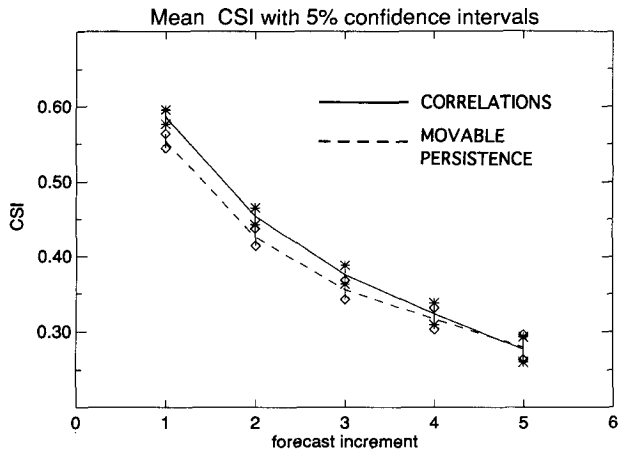


FIG. 15. Critical success index scores for correlations-based forecast (solid) and movable persistence (dots) as a function of forecast increment (each increment is 0.5 h). A CSI of 1.0 indicates a perfect forecast, and 0.0 denotes no skill.

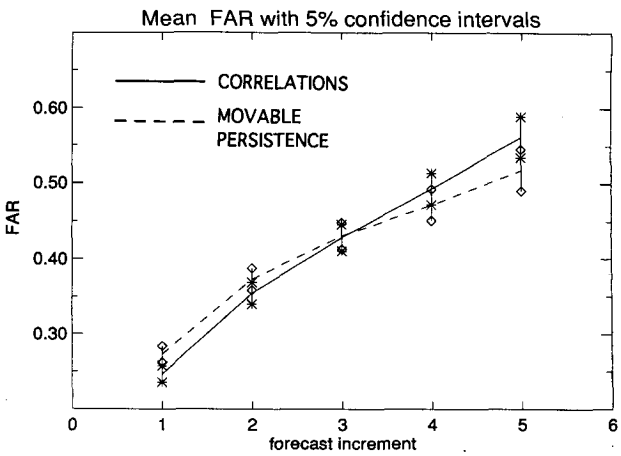


FIG. 17. FAR scores for correlations-based forecast (solid) and movable persistence (dots) as a function of forecast increment. A FAR of 0.0 indicates a perfect forecast, and 1.0 denotes no skill.

movable persistence for the longer forecasts, though not by a statistically significant amount. Figure 16 shows a similar trend for the POD, and Fig. 17 shows that the FAR scores for correlation are significantly better at the first time interval but become worse as time progresses, though not by a statistically significant amount.

Thus, we conclude that the correlations scheme exhibits skill over movable persistence for at least the first hour of the forecast. Because of this and because of the greater utility of the correlations scheme, which is not dependent on tracking contours that can split or merge, we conclude that it is a more appropriate algorithm for nowcasting of small features.

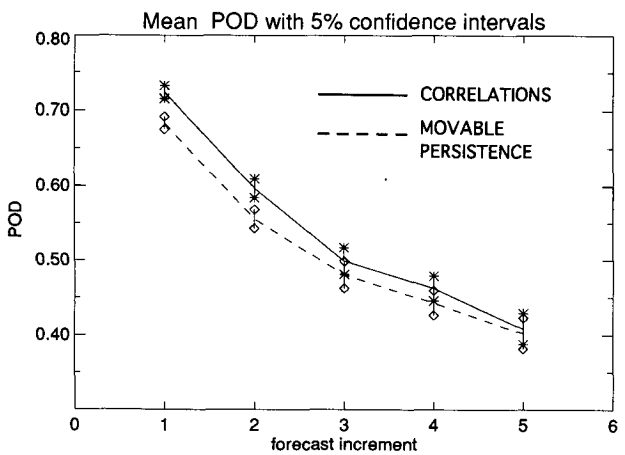


FIG. 16. POD scores for correlations-based forecast (solid) and movable persistence (dots) as a function of forecast increment. A POD of 1.0 indicates a perfect forecast, and 0.0 denotes no skill.

## 4. Conclusions

A cross-correlations-based cloud forecast technique has been developed that is skillful at extrapolating cloud features. The output is a set of synthetic (predicted) satellite images that may be looped in combination with analyzed images. Because the form of the output is identical to the input (pixel images), interpretation is easy. The scheme is clearly an improvement over persistence and gives the forecaster an informed, objective extrapolation of existing cloud features. The prototype scheme described here does have a number of limitations, including terrain advection, the inability to work well in convective situations, the tendency to smooth the forecast images with time, and occasionally, unrealistic looking images along inflow boundaries.

Some relatively simple but computationally intensive enhancements can be made to correct these problems, though the parameterization of developmental and dissipative effects is sure to prove challenging. Terrain advection can be eliminated through the coupling of the cloud forecast with a nephanalysis and background mask, advecting only the pixels determined to be cloudy. Boundary condition errors can be eliminated by widening the domain; smoothing effects could be mitigated by decreasing pixel size and eliminating the use of bilinear interpolation or by eliminating the iterative process and calculating all trajectory origins for every forecast frame as distinct points in the latest frame of satellite data. Some improvement may be gained by including conventional wind observations into the displacement vector analysis.

*Acknowledgments.* The authors would like to thank the careful reviews provided by Jean-Francois Louis, Ross Hoffman, and Ron Isaacs at AER, and Don Chisholm, Ken Heideman, Artie Jackson, and Stu Muench

at the Phillips Laboratory. Larry Knowlton helped generate test results. This research was supported by the U.S. Air Force under Contract F19628-92-C-0014.

## REFERENCES

Bellon, A., A. Kilambi, G. L. Austin, and M. R. Duncan, 1992: A satellite and radar rainfall observational and forecast system. Preprints, *Eighth Interactive Information and Processing Systems for Meteorology, Oceanography, and Hydrology,* Atlanta, GA, 67–74.

Benjamin, S. G., and N. L. Seaman, 1985: A simple scheme for objective analysis in curved flow. *Mon. Wea. Rev.,* **113,** 1184–1198.

Cressman, G. P., 1959: An operational objective analysis system. *Mon. Wea. Rev.,* **87,** 367–374.

Fuh, C.-S., and Maragos, P., 1991: Motion displacement estimation using an affine model for image matching. *Opt. Eng.,* **30,** 881–887.

Hamill, T. M., R. P. d'Entremont, and J. T. Bunting, 1992: A description of the Air Force Real-time Nephanalysis model. *Wea. Forecasting,* **7,** 288–306.

Heideman, K. F., H.-C. Huang, and F. H. Ruggiero, 1990: Evaluation of a nowcasting technique based on GOES IR satellite imagery. Preprints, *Fifth Conf. on Satellite Meteorology and Oceanography,* London, Amer. Meteor. Soc. 366–371.

Leese, J. A., and C. S. Novak, 1971: An automated technique for obtaining cloud motion from geosynchronous satellite data using cross correlation. *J. Appl. Meteor.,* **16,** 118–132.

Merrill, R. T., 1989: Advances in the automated production of wind estimates from geostationary satellite imagery. Preprints, *Fourth Conf. Satellite Meteorology and Oceanography,* San Diego, Amer. Meteor. Soc., 246–250.

Mitchell, K. E., and D. Hahn, 1989: Development of a cloud forecast scheme for the GL baseline spectral model. GL-TR-89-0343, Phillips Laboratory/Geophysics Directorate, Hanscom AFB, MA, 147 pp.

Nagle, R. E., 1992: A kinematic model for the short-term prediction of remotely sensed hydrometeors. NOARL Tech Note 210, Navy Oceanographic and Atmospheric Research Lab, Monterey, CA. 47 pp.

Nehrkorn, T., T. M. Hamill, and L. W. Knowlton, 1993: Nowcasting methods for satellite imagery. PL-TR-93-2021, Phillips Laboratory/Geophysics Directorate, Hanscom AFB, MA, 113 pp.

Panofsky, H. A., and G. W. Brier, 1968: *Some Applications of Statistics to Meteorology.* Pennsylvania State University, 153–157.

Ruggiero, F. H., K. F. Heideman, and J. Doherty, 1991: An evaluation of three techniques for nowcasting precipitation fields using weather radar. Preprints, *25th Conf. Radar Meteorology,* Paris, Amer. Meteor. Soc., 83–86.

Slingo, J. M., 1987: The development and verification of a cloud prediction scheme for the ECMWF model. *Quart. J. Royal Meteor. Soc.,* **113,** 899–927.

Staniforth, A., and J. Cote, 1991: Semi-lagrangian integration schemes for atmospheric models—A review. *Mon. Wea. Rev.,* **119,** 2206–2223.

Stanski, H. R., L. J. Wilson, and W. R. Burrows, 1989: Survey of common verification methods in meteorology. MSRB 89-5, Canadian Atmospheric Environment Service, Downsview, Ontario, 114 pp.

Sundqvist, H., E. Berge, and J. Kristjansson, 1989: Condensation and cloud parameterization studies with a mesoscale numerical weather prediction model. *Mon. Wea. Rev.,* **117,** 1641–1657.

Tuttle, J., and G. B. Foote, 1990: Determination of the boundary layer airflow from a single Doppler radar. *J. Atmos. Oceanic Technol.,* **7,** 218–232.